2024 IEEE/RSJ International Conference on Intelligent Robots and Systems (IROS)
October 14-18, 2024. Abu Dhabi, UAE

A 6-DOF Double-layer Programmable Remote Center of Motion Robot for Vitreoretinal Surgery

Chenyu Wang[1] and Seong Young Ko[2*]

***Abstract*— During vitreoretinal surgery, surgeons are required to precisely manipulate surgical tools within a confined workspace of an eye, which is roughly 2.5 cm spherical in shape. Because the surgical view can only be obtained by a microscope placed above the eyeball through the pupil, the eyeball needs to be moved or rotated during the operation to see a larger portion of the retina. At this point, general Remote Center of Motion (RCM) mechanisms require additional actuators or manual modification. On the other hand, a programmable RCM mechanism can reduce surgery time without a physical alignment procedure. This study introduces a novel six-degree-of-freedom (DoF) programmable RCM mechanism capable of generating the RCM at random positions in 3D space. Our approach combines two planar 5-bar linkage mechanisms placed in parallel, creating a double-layered configuration to establish the programmable RCM mechanism. We optimized the workspace of each planar mechanism to a customized workspace for a general eyeball model using genetic algorithms, focusing on maximizing the manipulability of the target workspace. The Phantom Omni device was utilized as a remote controller to remotely control the proposed mechanism in a transparent eyeball model with a diameter of 4 cm. Evaluation of the functionality of the programmable RCM mechanism at various RCM points showed that the overall error was less than 1 millimeter. The repeatability of the mechanism was tested and showed an accuracy of about 127 micrometers.**

I. INTRODUCTION

With the development of robot-assisted minimally invasive surgery (RA-MIS), surgical robots have played an important role in the surgical field due to their advantages over humans such as maintaining a posture for a long time, applying force detection, no tremor, etc. Vitreoretinal surgery is one of the most challenging procedures in ophthalmic operations. Surgeons are required to insert surgical instruments through an approximately 0.65mm trocar incision in the sclera[2] and manipulate them within the eyeball to conduct precise operations on the retina. At the same time, the surgical tool should not exert too much force on the sclera to void undesired damage to the tissue. This motion has been called a remote center of motion(RCM), the robot applied in the vitreoretinal surgery should have micro-level accuracy and millimeter-level RCM accuracy to conduct the required surgical procedure.

*This paper was supported by the National Research Foundation of Korea (NRF) grant funded by the Korean government (MSIT) (No.2022R1A2C2008422).

[1]C. Wang is with the Department of Mechanical Engineering, Graduate School, Chonnam National University, Gwangju, 61186, Republic of Korea (email: wcy1669840335@gmail.com).

[2]S. Y. Ko is with the School of Mechanical Engineering, Chonnam National University, Gwangju, 61186, Republic of Korea (corresponding author phone number: +82-62-530-1670; fax: +82-62-530-1689; e-mail: sko@jnu.ac.kr).

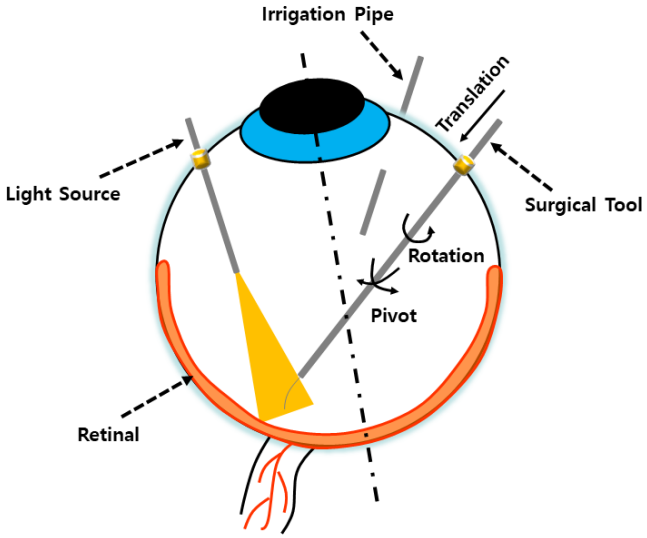

Fig. 1. Conceptual diagram of vitreoretinal surgery

A. The mechanical RCM mechanism

One of the ways to achieve the RCM is by using the mechanical constraint to limit the motion of the surgical tool to realize the RCM. One of the examples is the parallelogram mechanism [3]. The parallelogram mechanism can replicate the motion of the proximal joint into distal sides to generate micro-level precision RCM at a fixed point. The parallelogram mechanism can keep the actuators in the proximal area to reduce inertia and enhance accuracy and stability [4]. However, in actual ophthalmic surgical operations, it is crucial to access the surgical view through a microscope that is positioned right above the eyeball. To access a wider view of the retina, the eyeball needs to be moved or rotated during the operation. Thus, when the eyeball is rotated, the position of the robot's RCM should also change. For the mechanical RCM mechanisms (including a parallelogram mechanism or a spherical link mechanism, etc), a physical alignment process is required to change the trocar point manually. So, in this situation, we believe a programmable RCM will have a positive impact on shortening the operation time and reducing postoperative complications since it does not need physical alignment.

B. The programmable RCM mechanism

The second way is to use software constraints to build a programmable RCM. Several researchers have proposed some robotic systems with programmable RCM mechanisms. Weiwei et al. [5] proposed a dual-arm robotic system using

the Stewart-Gouph platform designed for performing ophthalmic surgeries. Each arm of this system incorporates a Stewart-Gough platform to generate the required six-degree-of-freedom (6-DoF) motion. M. Ali Nasseri et al. [6] proposed a novel ophthalmic surgical robot that is better adapted to the environment within the operating room for eye surgeries using a hybrid parallel–serial robot system. The robotic system comprises a pair of parallel coupled joint mechanisms (PCJMs), each PCJM consisting of two piezoelectric linear motors placed in parallel. With its straightforward design, the robotic system encompasses the 4-DoF motion required for eye surgery while maintaining high precision. Ali Uneri et al [7][8] proposed a new steady-hand surgery robot for ophthalmic surgery. This Steady-hands robot integrates an X-Y-Z stage to adjust the position of the RCM and adds a six-bar mechanical RCM mechanism at the end to provide the RCM motion. The robot is directly operated by surgeons, integrating adaptive control to counteract any additional tremors in the surgeon's hands to enhance precision.

In this work, we will build a new programmable RCM mechanism with sufficient workspace to obtain a larger pivot range even after changing the RCM point. The proposed system needs to have RCM error less than 1mm and robot tip precision under less 25μm, since the average thickness of the retina is 250μm[9], to achieve high-quality motion around the RCM motion in 3D space.

The rest of this article is organized as follows. Section II introduces the mechanical design of the double-layer 5-bar linkage mechanism and its actuation system. Section III introduces the kinematics analysis of the proposed mechanism. Section IV demonstrates the optimization of each parameter of the proposed design based on the surgical environment and surgery requirement. Section V details the remote control system applied to control the proposed robot remotely. Section VI analyzes the RCM motion error of the proposed robot mechanism. Finally, Section VII concludes this article.

II. MECHANICAL DESIGN

A. Overall System Design

As depicted in Fig. 3(a), the figure presents the conceptual design of the proposed double-layer 5-bar linkage mechanism. The pivoting motion of the surgical tool will be generated by the two 5-bar linkage mechanisms placed in parallel. Two tip points of the planar mechanism will be connected to each other to build a platform that can attach various surgical tools and actuators.

Fig.2 shows the mechanical design of the double-layer 5-bar linkage mechanism. A linear guide is incorporated to connect two 5-bar linkage mechanisms to compensate for the distance changing between two tip points of the planar mechanism. An additional linear motor and a rotary motor have been attached to facilitate the insertion and axial rotary motion of the end-effector. The upper mechanism connects with the slider which is attached to the linear guide using a universal joint, and the lower mechanism connects with the linear guide using a spherical joint(Magnetic ball joint K-8, MAGNA.co.LTD.).

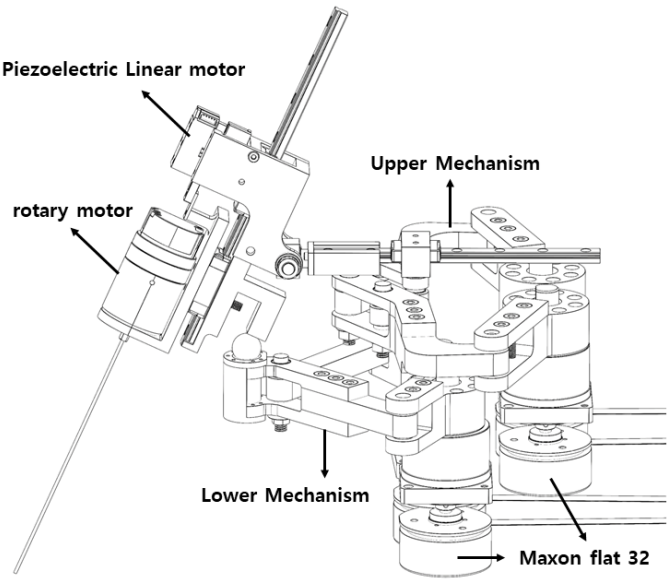

Fig. 2. The hardware design of the proposed double-layer 5-bar mechanism.

B. Design of the upper 5-bar linkage Mechanism

The upper mechanism of the proposed robot is a 5-bar linkage with an extra middle link as shown in Fig 3(b). This is a modification of the conventional 5-bar linkage, achieved by adding two links to form a diamond shape with two distal links c_1. An additional link is then used to connect the two endpoints, creating an additional protruding endpoint P_1 that facilitates the connection to the 2-DoF end-effector. Consequently, the extra link will still be in the center of the two distal links of the 5-bar linkage. The workspace of this modified mechanism has a symmetric shape as the workspace of the conventional 5-bar linkage mechanism.

C. Design of the Lower 5-bar Linkage Mechanism

As illustrated in Fig.3(c), the lower mechanism of the proposed mechanism is a 5-bar linkage with an extended link. The model simply extended one of the distal links of the 5-bar linkage mechanism to facilitate the connection with the ball joint. In order to prevent the backlash and plays inside the joints caused by uncertain connections between the links, all precision bearings and screws were used in all joint designs to ensure a good connection of the links, increasing the precision of the whole mechanism. At the final tip of the 5-bar linkage mechanism with the link, there is a magnetic ball joint that has large possible tilting angles to satisfy the requirement of the whole mechanism.

D. Design of the Actuation Unit

In order to reduce the error caused by the motor's backlash, the high precision EC motors (Maxon EC 32 flat with Hall sensor, Maxon motor) with harmonic drive gear reductions (CSF-8-100-2XH-J,100:1 Gear ratio, Samick HDS co.) are used, characterized by a resolution under than 1 micro-rad. EPOS4 controllers (EPOS4 Compact 24/1.5,

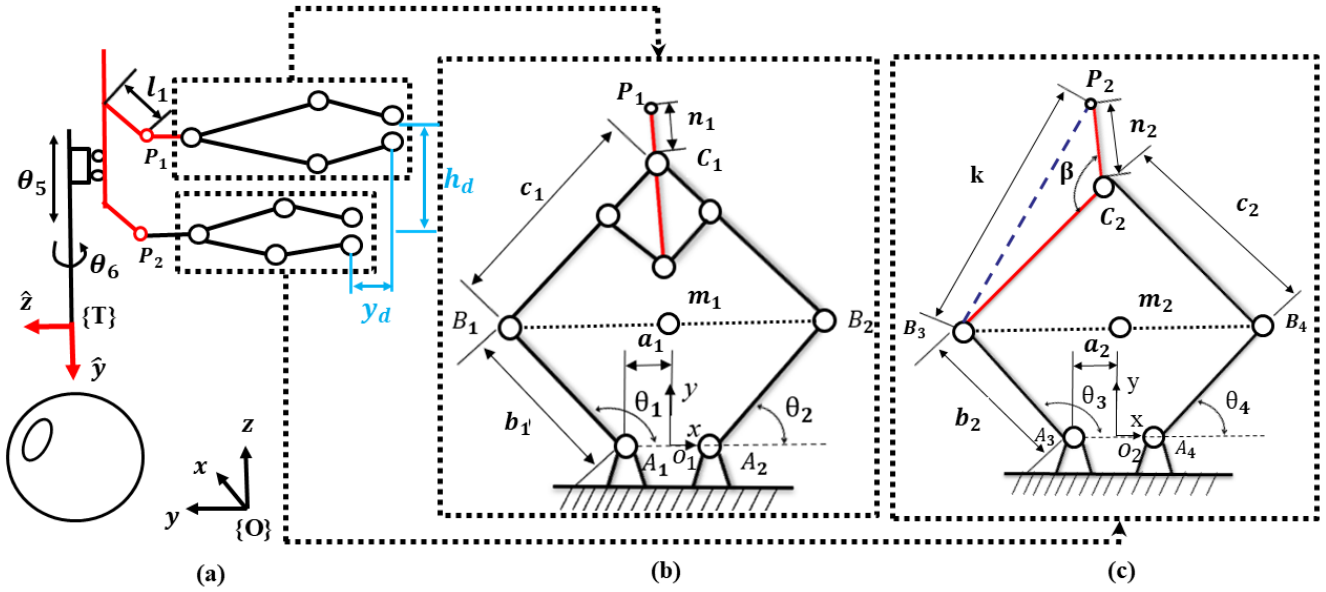

Fig. 3. (a) The conceptual design of the double-layer 5-bar linkage mechanism (b) kinematics specifications of the upper mechanism (c) kinematics specifications of the lower mechanism

Maxon motor) were used to control the motors. In addition, the linear actuation in the end-effector (EE) utilizes a piezo-linear motor (Piezo LEGS® Linear LT40), resulting in a resolution of less than 1 nm. The rotation at the end tip is actuated by a piezo rotary motor (Piezo LEGS® LR 23-50).

III. KINEMATICS MODELING

In this section, the kinematics modeling of the double-layer 5-bar linkage mechanism is presented.

A. Kinematics of the upper mechanism

Fig.3(b) shows the sketch of the upper 5-bar linkage mechanism. The geometric relationship between the final tip position O_1P_1 = $[x_1\ y_1]$ and the input joint angles is derived as:

$$(x' - b_1\cos(\theta_1) + a_1)^2 + (y' - b_1\sin(\theta_1))^2 = c_1^2 \quad (1)$$

$$(x' - b_1\cos(\theta_2) - a_1)^2 + (y' - b_1\sin(\theta_2))^2 = c_1^2 \quad (2)$$

where

$$x' = x_1 - n_1\sin(\beta_1) \quad (3)$$

$$y' = y_1 - n_1\cos(\beta_1) \quad (4)$$

$$\beta_1 = \tan^{-1}\left(\frac{b_1(\sin(\theta_1) - \sin(\theta_2))}{b_1(\cos(\theta_1) - \cos(\theta_2)) + 2a_1}\right) \quad (5)$$

For the forward kinematics of the upper mechanism, the end tip position is obtained as follows:

$$P_1 = \begin{bmatrix} m_{1x} + (d + n_1)\cos(\frac{\pi}{2} + \beta_1) \\ m_{1y} + (d + n_1)\sin(\frac{\pi}{2} + \beta_1) \end{bmatrix} \quad (6)$$

where

$$m_{1x} = \frac{b_1(\cos(\theta_1) + \cos(\theta_2))}{2} \quad (7)$$

$$m_{1y} = \frac{b_1(\sin(\theta_1) + \sin(\theta_2))}{2} \quad (8)$$

where the m_1 is the midpoint of the line B_1B_2. The value of d is the length of the line C_1m_1.

B. Kinematics of the lower mechanism

Fig. 3(c) shows the sketch of the lower 5-bar linkage mechanism. The geometric relationship between the final tip position O_2P_2 = $[x_2\ y_2]$ and the input joint angles is derived as follows:

$$(x_2 - b_2\cos\theta_3 + a_2)^2 + (y_2 - b_2\sin\theta_3)^2 = k^2 \quad (9)$$

$$(C_{2x} - b_2\cos\theta_4 - a_2)^2 + (C_{2y} - b_2\sin\theta_4)^2 = c_2^2 \quad (10)$$

where the length of k and the position of O_2C_2 = $[C_2x\ C_2y]$ can be calculated by using the Law of Cosines since n_2, c_2 and β are known value. For the forward kinematics of the lower mechanism, the position of the point C_2 is calculated as the equation (6) to (8), and the position of the point P_2 is obtained by using the $\triangle P_2B_3C_2$.

C. Kinematics of the parallel configuration

The two 5-bar mechanisms are interconnected via a linear guide and a slider. Each planar mechanism connects with the end-effector with a universal joint and a spherical joint, respectively. Consequently, as shown in Fig 3, the segment represented by the red line forms a parallelogram lying within a same plane. Forward kinematics can also be calculated using the geometric relationship.

For the forward kinematics of the proposed double-layer configuration, the direction of the offset l_1 will follow the tip direction of the upper mechanism due to the universal joint.

$$(T_x, T_y, T_z, \alpha, \beta, \gamma) = f_{FK}(\theta_1, \theta_2, \theta_3, \theta_4, \theta_5, \theta_6) \quad (11)$$

As a result, the middle link m_1P_1 of the upper mechanism, the offset l_1 and the end-effector are still in the same plane

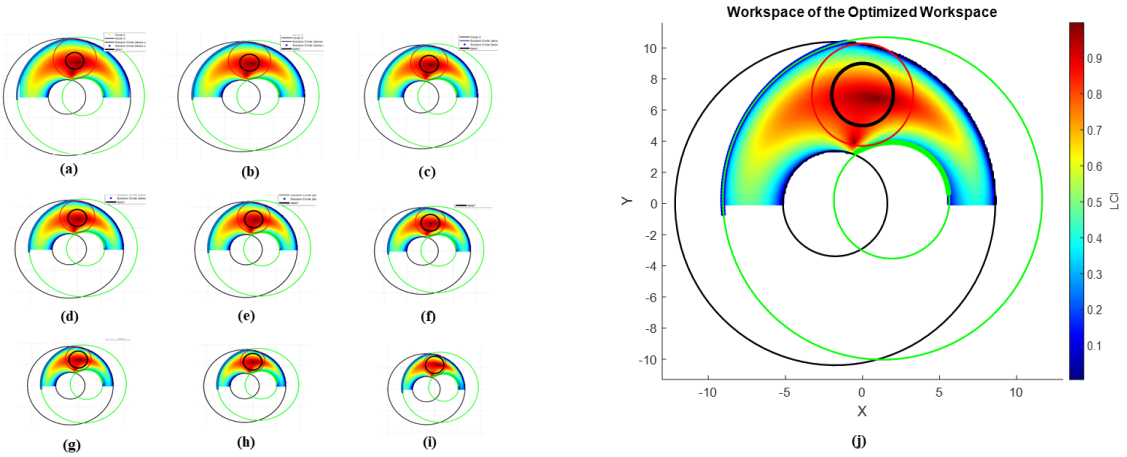

Fig. 4. The workspace of the optimization result. The workspace is visualized with different colors according to LCI value, where the red color indicates the points with a high manipulability index and the blue color indicates the points with a bad manipulability index. (a) to (i) is the optimization result with different penalty factors from penalty = 0.001 to 0.07. As the penalty increases, the optimization result becomes smaller until the maximum inscribed circle becomes the same size as the target workspace. (j) optimization result of the lower mechanism when the penalty factor = 0.02

to form the mechanism. The geometric relationship can be shown as :

$$\vec{OT} = \vec{OP_1} + \vec{L_1} + \vec{P_1P_2} + \theta_5 \frac{\vec{P_1P_2}}{|\vec{P_1P_2}|} \tag{12}$$

where the $\vec{OP_1}$ is the tip vector of the upper mechanism, $\vec{L_1}$ is the vector of the offset, $\vec{P_1P_2}$ is the vector between two tip of planar mechanism, respectively. By defining the direction of the sliding rail as the y-axis of the EE and the direction of the vector L_1 to be the z-axis of the EE, so the direction of the end-tip point of the entire mechanism can be represented as [$\hat{x}$, $\hat{y}$, $\hat{z}$].

For the remote control, the inverse kinematics of the proposed mechanism is required. As shown in Fig. 3, the tip point of the mechanism is $\vec{OT}$ = [x, y, z], and the direction is [$\hat{x}$, $\hat{y}$, $\hat{z}$]. The tip point of the upper mechanism is OC_1= [x' y']. The input angles of the upper mechanism are [θ_1 θ_2] which is calculated by solving the simultaneous equations as below:

$$f_1 = (x' - b_1\cos\theta_1 + a_1)^2 + (y' - b_1\sin\theta_1)^2 = c_1^2 \tag{13}$$

$$f_2 = (x' - b_1\cos\theta_2 - a_1)^2 + (y' - b_1\sin\theta_2)^2 = c_1^2 \tag{14}$$

$$f_3 = OT + R_{\text{without }\theta_6} * TP_1 - OP_1 \tag{15}$$

The tip point of the lower mechanism is represented as:

$$OP_2 = OT + R_{\text{without }\theta_6} * TP_2 \tag{16}$$

where the [x' y'] is obtained using equations (3) to (5) and $R_{\text{without }\theta_6}$ is the rotation matrix between global coordinate system and the end-effector of the robot system without the rotation of the end-effector.

IV. Optimization of Robot Mechanism

A. Planar mechanism optimization

The double-layer mechanism in our design employs two planar mechanisms to control the pivoting motion under RCM constraints. The generation and effectiveness of the pivoting motion, as well as the functionality of the Remote Center of Motion (RCM), are linked to the size and position of the two planar workspaces. To get customized sizes of workspace with the highest manipulability, we first define the maximum inscribed circle and then employ genetic algorithms to optimize the target workspace within the entire usable area of the planar workspace. In this study, the objective function is defined as the total condition index (TCI), which is the average of the local condition index (LCI) of all points within the target workspace under a specific link range.

$$x = max(TCI - x_{pen}), \quad TCI = \frac{1}{W}\sum_{i=1}^{W} LCI(p)$$

$$where \quad LCI = \frac{1}{k(J)}, \quad k(J) = \frac{\sigma_{max}(J)}{\sigma_{min}(J)} \tag{17}$$

Where the J is the Jacobian matrix of the planar mechanism, and σ_{max} and σ_{min} are the maximum singular value and minimum singular value of the Jacobian matrix of the planar mechanism. Then, TCI is obtained by calculating the average of LCI values inside the target workspace. W is the amount of the sample points inside the target workspace and p is the points inside the target workspace. In order to avoid the huge values of link combination results from the optimization, we introduced a penalty λ which is proportional to the sum of the links b and c :

$$x_{pen} = \lambda(b_1 + c_1) \tag{18}$$

For the optimization of the lower mechanism, the b_2, c_2 and β (see Fig. 3(c)) were set as optimization parameters because the length of the link a_2 is limited by the motor size and it needs to be as small as possible according to research related to the 5-bar linkage mechanism in literature [12][13].

So for any link combination, we used the forward kinematics to draw the boundary of the workspace of the mechanism

and fit them with a circle. The maximum inscribed circle was defined as the workspace of the mechanism by finding the largest circle tangent to the workspace boundary. After that, the target workspace along the y-axis will be searched to become the best target workspace based on the TCI.

In the configuration of the Genetic Algorithm (GA) employed for the optimization process, we set a population size of 50 to balance computational efficiency and the elite number was set to 5. The entire optimization process was completed within approximately 1.5 hours with 0.01 cm resolution.

The optimization results of lower mechanism varying with different penalty factors λ are illustrated in Fig. 4(a) to (i). The size of the target workspace was set as a circle with a 2cm diameter. We observe that as the penalty factor increases, the resulting workspace size decreases. Notably, when the penalty factor exceeds 0.07, the target workspace size reduces to touch the maximum inscribed circle.

In the optimization, we selected a penalty factor λ = 0.02 as the optimal value. This choice is based on the observation that with this penalty factor, the target workspace ideally encompasses the entire red region of the workspace. The red region signifies areas of high manipulability, indicating that this penalty factor effectively balances workspace size with manipulability.

With the selected penalty factor λ, the result of the links b_2, c_2 and β were obtained as b_2 = 3.4916, c_2 = 6.3158 and β = 2.0014. The workspace of the mechanism of the optimized link combination is shown in Fig.4(j). It is evident from the figure that the black circle, which indicates the target workspace, is situated within the red area of the overall workspace. This red area denotes regions of the workspace that are favorable (with an LCI greater than 0.7). The average LCI inside the target workspace is 0.89. and the target workspace centered at [0, 6.83].

Regarding the optimization of the upper mechanism, the length of the linkage a_1 was also minimized as discussed above. The center of the target workspace has been limited at [0, 10] which is right above the center of the lower mechanism due to the offset y_d (see Fig.3). Eventually, the parameters to be optimized are b_1, c_1, and n_1. By using the same GA setting for the lower mechanism, the final results were obtained as b_1 = 5.4921, c_1 = 8.5394, and n_1 = 2.2982, resulting in the maximum TCI = 0.871.

V. Remote Control of Proposed Robot

A. Remote control configuration

In this section, the remote control system is present. To manage the 6-DoF proposed mechanism, the Phantom Omni haptic device is utilized as the remote controller. It is defined so that the pen-shaped end-effector of Phantom Omni system aligns with the end-effector of the double-layer 5-bar linkage mechanism.

B. Control Architecture

The final surgical procedures will be performed in various motion modes of the double-layer 5-bar linkage mechanism, with switching between the different modes implemented by buttons on the Phantom Omni haptic device. Communication between the robot controller and the remote controller is implemented within the robot operating system 2 (ROS2) environment running on a Ubuntu operating system, with a control loop set to intervals of 10ms.

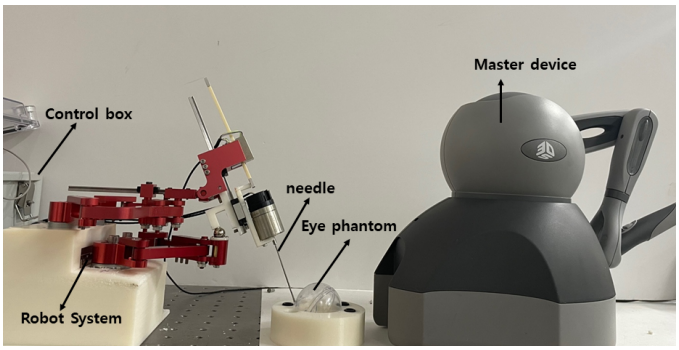

Fig. 5. Experimental Setup of the remote control.

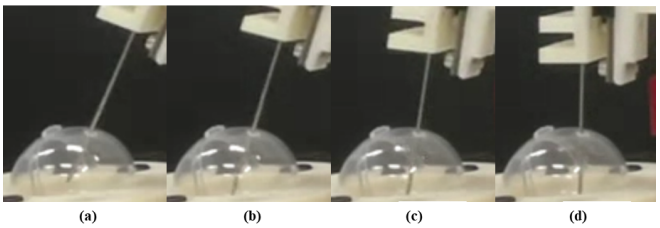

Fig. 6. Demonstration of the RCM motion using the proposed mechanism.

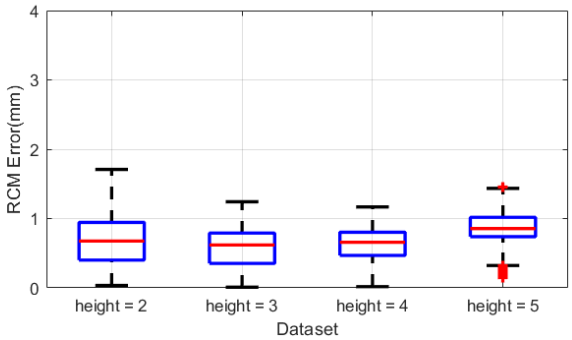

Fig. 7. RCM error with different heights of the RCM position. The maximum error of the RCM is 1.704mm and the average RCM error is 0.691mm.

C. RCM realization

The desired position of the proposed robot is calculated by using the pen-shaped end-effector of the Phantom Omni device. The robot joint values are consecutively updated through inverse kinematics calculations. When the RCM mode needs to be activated, the tip of the Phantom Omni device is moved the surgery robot to the desired RCM point and the force feedback mode of the Phantom Omni device is activated. Then, the point where the last three joints intersect is set to RCM point, thus the operator can feel the inserting point is restricted. In this way, the EE of the Phantom Omni can give the RCM information to the surgery robot to solve the inverse kinematics.

VI. Experiment Results

In this section, experimental results and analysis are provided. We mainly tested the accuracy of the proposed robot system since precision is the most important index for its application.

A. RCM error evaluation

To comprehensively evaluate the RCM capability of the proposed robotic system under varying conditions, we conducted a series of experiments to test the error on RCM motion according to different RCM heights. The experimental setup is shown as Fig. 5. The eyeball phantom used in this experiment is a transparent plastic ball placed in a socket to allow the free rotation of the eyeball. The surgical tool is inserted through the trocar with a diameter of 3 mm and moves to generate the RCM motion around the trocar point. The poses of the robot are recorded by using the Polaris Spectra (NDI Inc. 3D tracking system). The marker was attached in the linear guide as shown in the movie clip provided in Supplementary Media. As shown in Fig. 7, the RCM error did not exceed 1.704 mm throughout the whole process. More importantly, most of the errors were measured to within 1 mm, represented by the box portion of the plot in Fig. 7, indicating that the RCM errors were less than 1 mm. This also shows that the RCM error is not significantly affected by the height of the RCM positions. These findings highlight the robustness and consistency of the RCM capabilities of the proposed robotic system at different operational heights, confirming its suitability for precise surgical applications

B. Repeatability Test

For the repeatability test, we selected seven points within the target workspace of the mechanism. Then the robot moved to each of these points from six different directions. In the repeatability test, a camera was used to determine whether the robot tip reached the target positions, with a resolution of 13.2μm per pixel. After completing the testing process, the averaged repeatability was measured to be 127 μm.

VII. Conclusion

In this study, a novel mechanical structure for vitreoretinal surgery is presented, which is designed by using two 5-bar linkage mechanisms in parallel. Workspace analysis and the optimization of link lengths were conducted on both individual 5-bar linkage mechanisms to guarantee excellent manipulability. The average LCIs inside the target workspace for the upper mechanism and the lower mechanism were obtained to be 0.89 and 0.87, respectively. The RCM implementation of the proposed mechanism was tested through experiments. The maximum error of the RCM was measured to be 1.704 mm and the average RCM error was 0.691 mm, which showed the robot's feasibility, despite the tight accuracy requirements and confined workspace in vitreoretinal surgery.

For vitreoretinal surgery, the required precision of the robot tip is within 25μm for all possible operations as mentioned in Section I. So in the future, the accuracy of the whole robot will be further improved using an anti-backlash mechanism or flexure hinge joints. The additional mechanism to integrate the surgical tool (such as a gripper) will be designed and implemented. We will verify the feasibility of the robotic system by applying it to several surgical procedures requiring high precision, such as membrane peeling.

References

[1] I. I. Iordachita, M. D. De Smet, G. Naus, M. Mitsuishi, and C. N. Riviere, "Robotic assistance for intraocular microsurgery: Challenges and perspectives," *Proceedings of the IEEE*, vol. 110, no. 7, pp. 893-908, 2022.

[2] N. Wang, X. Zhang, M. Li, H. Zhang, D. Stoyanov, and A. Stilli, "A 5-DOFs Robot for Posterior Segment Eye Microsurgery," in *IEEE Robotics and Automation Letters*, vol. 7, no. 4, pp. 10128-10135, Oct. 2022,

[3] A. Gijbels, N. Wouters, P. Stalmans, H. Van Brussel, D. Reynaerts and E. V. Poorten, "Design and realisation of a novel robotic manipulator for retinal surgery." *IEEE/RSJ International Conference on Intelligent Robots and Systems*, Tokyo, Japan, 2013, pp. 3598-3603

[4] Smits J, Reynaerts D, Vander Poorten E, "Synthesis and methodology for optimal design of a parallel remote center of motion mechanism: Application to robotic eye surgery." *Mechanism and Machine Theory.*, 151: 103896, 2020.

[5] W. Wei, R. E. Goldman, H. F. Fine, S. Chang and N. Simaan, "Performance Evaluation for Multi-arm Manipulation of Hollow Suspended Organs." *IEEE Transactions on Robotics.*, vol. 25, no. 1, pp. 147-157, Feb. 2009.

[6] M. A. Nasseri et al, "The introduction of a new robot for assistance in ophthalmic surgery." *35th Annual International Conference of the IEEE Engineering in Medicine and Biology Society (EMBC)*, Osaka, Japan, 2013, pp. 5682-5685

[7] A. Üneri, M. A. Balicki, J. Handa, P. Gehlbach, R. H. Taylor and I. Iordachita, "New steady-hand Eye Robot with micro-force sensing for vitreoretinal surgery." *3rd IEEE RAS & EMBS International Conference on Biomedical Robotics and Biomechatronics*, pp. 814-819, 2010

[8] A. Ebrahimi et al, "Stochastic Force-Based Insertion Depth and Tip Position Estimations of Flexible FBG-Equipped Instruments in Robotic Retinal Surgery." *IEEE/ASME Transactions on Mechatronics*, vol. 26, no. 3, pp. 1512-1523, June 2021.

[9] M. Zhou et al, "Towards Robotic-Assisted Subretinal Injection: A Hybrid Parallel–Serial Robot System Design and Preliminary Evaluation." *IEEE Transactions on Industrial Electronics*, vol. 67, no. 8, pp. 6617-6628, Aug. 2020

[10] Cabrera J A, Simon A, Prado M, "Optimal synthesis of mechanisms with genetic algorithms." *Mechanism and Machine Theory*, vol. 37, no. 10, pp. 1165-1177, 2002.

[11] Leal-Naranjo, José-Alfredo, et al, "Multi-objective optimization of a parallel manipulator for the design of a prosthetic arm using genetic algorithms." *n Latin American Journal of Solids and Structures*, vol. 15, 2018.

[12] Xin-Jun Liu, Jinsong Wang, G. Pritschow, "Kinematics, singularity and workspace of planar 5R symmetrical parallel mechanisms." *Mechanism and Machine Theory*, vol. 41, no 2, pp. 145-169, 2006.

[13] Xin-Jun Liu, Jinsong Wang, Hao-Jun Zheng, "Optimum design of the 5R symmetrical parallel manipulator with a surrounded and good-condition workspace." *Robotics and Autonomous Systems*, vol. 54, no 3, pp. 221-233, 2006